FUDMA Journal of Sciences (FJS)
ISSN online: 2616-1370
ISSN print: 2645 - 2944
Vol. 8 No. 3, June, (Special Issue) 2024, pp 581 - 597
DOI: https://doi.org/10.33003/fjs-2024-0803-2656

INFLUENCE OF SINTERING TEMPERATURE ON STRUCTURAL PROPERTIES OF HEMATITE (Fe_2O_3) NANOPARTICLES AND ITS APPLICATION FOR ELECTROMAGNETIC INTERFERENCE SHIELDING

***[1]Idris Muhammad Chiromawa, [1]Ibrahim Garba Shitu, [1]Aminu Muhammad,**
[2,3]Kamil Kayode Katibi and [1]Sani Garba Durmin Iya

[1]Department of Physics, Faculty of Natural and Applied Sciences, Sule Lamido Universiti Kafin Hausa, Jigawa State, 048, Nigeria.
[2]Department of Physics, Faculty of Science, Universiti Putra Malaysia, UPM Serdang, Selangor 43400, Malaysia.
[3]Department of Agricultural and Biological Engineering, Faculty of Engineering and Technology, Kwara State University, Malete, 23431, Nigeria.

*Corresponding authors' email: idrismc@slu.edu.ng

ABSTRACT

Hematite (Fe_2O_3) nanoparticles have garnered significant attention due to their exceptional magnetic properties and potential applications in advanced technologies, including electromagnetic interference (EMI) shielding. Optimizing these properties through controlled synthesis methods is essential for enhancing their performance in such applications. This study explores the impact of sintering temperature on the structural, magnetic, and EMI shielding properties of hematite nanoparticles synthesized via an auto-combustion method. It was found that increasing sintering temperatures led to a consistent growth in crystallite size, as confirmed by multiple X-ray diffraction (XRD) techniques, including Scherrer's method, the Williamson-Hall methods (UDM, USDM, UDEDM), the Monshi-Scherer Method (MSM), the Size-Strain Plot (SSP) method, the Halder-Wagner method (HWM), and further validated by Field Emission Scanning Electron Microscopy (FESEM) analysis. The nanoparticles exhibited superparamagnetic behaviour with a saturation magnetization (Ms) of 4.0 emu/g, making them particularly advantageous for EMI shielding applications. Furthermore, Fe_2O_3 nanoparticles were embedded into a polyvinyl alcohol (PVA) matrix to fabricate nanocomposite films, which demonstrated significant improvements in EMI shielding effectiveness. The reflection and absorption losses were enhanced with increasing Fe_2O_3 content, indicating the nanocomposites' strong capability to attenuate electromagnetic waves. This study underscores the critical role of sintering temperature in optimizing the structural and magnetic properties of hematite nanoparticles, making them highly suitable for advanced technological applications, especially in electromagnetic interference shielding.

Keywords: Hematite (Fe_2O_3), Nanoparticles, Sintering Temperature, Electromagnetic Interference (EMI) Shielding, Auto-Combustion, Crystallite Size

INTRODUCTION

Hematite nanoparticles, specifically α-Fe_2O_3, have emerged as highly attractive nanomaterials with extensive applications in the scientific and technical realms. These nanoparticles possess a range of desirable properties, including thermodynamic stability, low cost, non-toxicity, and exceptional magnetic, electronic, photonic, and optical characteristics(Liu *et al.* 2018). Consequently, hematite nanoparticles have found utility in various fields such as gas sensors, biomedical applications, photo anodes, paints, catalysis, building materials, and Li-ion batteries. In the realm of nanomaterials, nanoscale particles (ranging from 1 to 100 nm) exhibit distinct physical properties that differ significantly from their micron-sized counterparts (10-100 µm)(Vallés *et al.* 2019). These nanoscale particles demonstrate diverse and intriguing attributes such as magnetic behaviour, optical properties, and surface reactivity, which are inherently linked to their particle size. Thus, to gain a comprehensive understanding of nanoscale material properties, accurate calculation of crystallite size becomes imperative (Xu *et al*. 2019).

Among the available methods for crystallite size determination, Scherrer's method is a well-established approach that employs X-ray diffraction (XRD) patterns to calculate the average size of crystallites based on the width of the diffraction peak. However, it is important to note that Scherrer's formula only provides a lower bound estimation of the crystallite size, as it overlooks the peak broadening contributions stemming from crucial factors like inhomogeneous strain and instrumental effects (Joseph *et al* 2018; Mohanapriya *et al.* 2020) . Consequently, if the peak broadening resulting from these factors were non-existent, the peak width would solely be determined by the crystallite size. In reality, both the crystallite size and lattice strain contribute to the broadening of X-ray diffraction peaks in nanoparticles. Lattice strain-induced peak broadening primarily arises from the significant volume of grain boundaries present in the nanoparticles (Zeng *et al* 2017). Thus, the strain existing within the nanomaterials can potentially influence the accurate calculation of the crystallite size. Consequently, to correctly measure the crystallite size and study the modifications introduced by strain in the properties of nanomaterials, strain calculations are required Mondal *et al* 2016). In contrast to Scherrer's method, X-ray diffraction peak profile analysis (XPPA) considers peak broadening arising from these aforementioned factors. This analytical method has been widely employed to determine grain size, lattice distortion, twinning, stacking fault probabilities, and long-range and root mean square stresses in nanocrystalline materials (Mondal *et al* 2016)

Various XPPA analytical methods, such as the Williamson-Hall methods, Stress-Strain Plot Methods, and Halder Wagner Methods, have been utilized to estimate the crystallite size and lattice strain in materials based on X-ray peak broadening. The current study aims to calculate the crystallite size of nanocrystalline sintered hematite nanoparticles using powder

X-ray diffraction data. This calculation takes into account the contributions of important factors, namely instrumental and lattice strain effects, to the broadening of X-ray peaks. Additionally, other microstructural parameters such as lattice strain, lattice deformation stress, and deformation energy density present in the nanoparticles are estimated using XPPA methods, particularly Williamson-Hall plots employing UDM, USDM, UDEDM models, and the Stress-Strain Plot Model. Furthermore, the crystallite size derived from X-ray diffraction data will be compared with the particle size distribution obtained from TEM analyses to validate the results.

MATERIALS AND METHODS

Materials

The materials used in the present research include iron (III) nitrate hydrate Fe $(NO_3)_3{\cdot}9H_2O$ (MW: 404.00; CAS: 7782-61-8), anhydrous citric acid ($C_6H_8O_7.H_2O$) (M_W: 192.12; CAS: 77-92-9), as starting materials and were of analytical grade. Distilled water was used to prepare aqueous solutions during the whole experiment.

Characterization

The Powder X-ray diffraction (PXRD) patterns for hematite nanoparticles, synthesized via the auto-combustion method, were recorded using an X-ray diffractometer with CuKα radiation, covering the 2θ range of 20° to 80°. Concurrently, the PXRD analysis of the PVA/Fe_2O_3 nanocomposite film was performed within the broader 2θ range of 10° to 80°. Fourier Transform Infrared (FTIR) spectroscopy (IRTracer-100, Shimadzu) was utilized to examine the chemical composition across the wavenumber range of 500-4000 cm^{-1}. Electrical impedance measurements were carried out at room temperature using a ZIVE SP1 electrical workstation (WonA Tech, Seoul, Korea) over a frequency range of 10 Hz to 1 MHz. The electromagnetic shielding effectiveness was evaluated using X-band waveguides connected to a vector network analyser (8510C, Agilent) operating within the 8-12 GHz frequency range. This comprehensive suite of analyses was designed to thoroughly characterize the structural, chemical, electrical, and electromagnetic shielding properties of the hematite nanoparticles and the PVA/Fe_2O_3 nanocomposite film.

Synthesis of Hematite (Fe_2O_3) using Auto-Combustion Technique

Hematite (Fe_2O_3) nanoparticles were synthesized using an auto-combustion method, employing iron (III) nitrate hydrate ($Fe(NO_3)_3{\cdot}9H_2O$) and citric acid ($C_6H_8O_7{\cdot}H_2O$) as the starting materials, with distilled water and ethanol serving as solvents. Precise amounts of the starting precursors were accurately measured using a precision balance. Iron (III) nitrate was dissolved in 50 ml of distilled water and stirred magnetically for 20 minutes to form a well-mixed solution. To enhance the reduction process, ethanol was added to the solution. A small amount of ammonia solution (NH_4OH) was then added dropwise with continuous stirring at room temperature to adjust the pH to 7. Citric acid was subsequently introduced in a stoichiometric ratio of 1:2 relative to the metal salt. The mixture was then heated at 80°C for 2 hours with continuous stirring, resulting in a homogeneous solution. This solution was heated to 110°C to convert the sol into a red gel, which was further heated to 250°C to initiate combustion. The resulting powder was then subjected to a sintering process at 550°C for 5 hours to eliminate any remaining organic components, yielding dried, single-phase hexagonal hematite nanoparticles (Fe_2O_3). The final product was then sintered at various temperatures: 200°C, 300°C, 400°C, and 500°C to study the effects of sintering temperature on the structural and magnetic properties of the nanoparticles.

Synthesis of PVA/Fe_2O_3 Nanocomposite

The nanocomposite film of PVA/Fe_2O_3 was fabricated using a straightforward solution casting method. Initially, polyvinyl alcohol (PVA) was fully dissolved in 15 ml of distilled water by gently stirring at 150 rpm for 3 hours at 80°C. Meanwhile, Fe_2O_3 nanoparticles, previously sintered at 500°C, were dispersed in 5 ml of distilled water and subjected to sonication for 30 minutes to ensure uniform dispersion. The dispersed Fe_2O_3 nanoparticles were then gradually added dropwise to the PVA solution, and the combined mixture was stirred for an additional hour to achieve a homogeneous blend. The resulting mixture was poured into a petri dish and allowed to dry at room temperature for 48 hours. Once dried, the nanocomposite film was carefully peeled from the petri dish and prepared for subsequent characterization. This method effectively produced a well-defined PVA/Fe_2O_3 nanocomposite film, making it suitable for further analysis and potential applications.

RESULTS AND DISCUSSION

X-ray Diffraction (XRD)

Figure 1 presents the X-ray diffraction (XRD) profile of the synthesized hematite nanoparticles, revealing distinct peaks at specific angles: 24.12°, 33.14°, 35.60°, 40.85°, 49.45°, 54.0°, 57.5°, 62.44°, 64.00°, 72.86°, and 75.35°. These peaks correspond to the crystal planes (111), (220), (311), (222), (400), (422), (511), (440), (214), (300), (1010), and (220), respectively. Notably, these peaks closely match the stick pattern of hexagonal hematite nanoparticles catalogued in the International Crystallographic Diffraction Data (ICDD) under the reference number 00-024-0072. The absence of impurity peaks in the diffractogram indicates the high purity of the synthesized particles. Moreover, the sharpness of the diffraction peaks suggests that the nanoparticles are highly crystalline. Based on this diffraction profile, essential structural parameters such as crystallite size, intrinsic strain, and stress will be calculated using various analytical models, as outlined in the following sections, to provide a comprehensive understanding of the structural properties of the synthesized hematite nanoparticles.

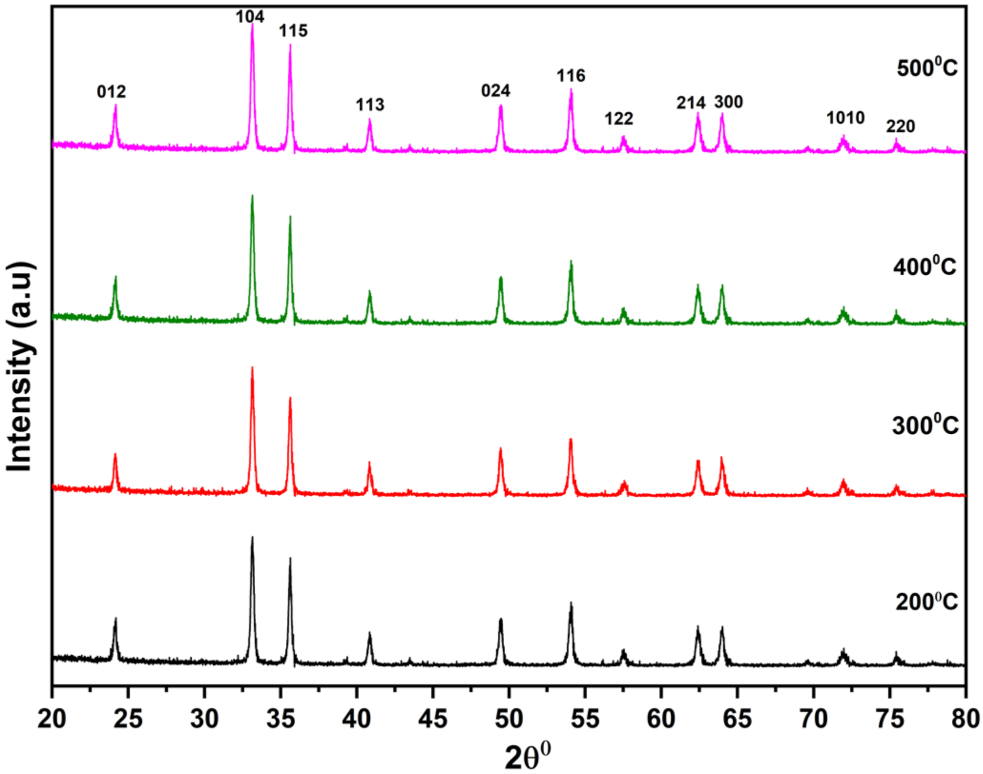

Figure 1: X-ray diffraction pattern of Fe_3O_4 nanoparticle at different sintering temperature.

X-ray Diffraction of Fe_3O_4/PVA Nanocomposite

X-ray diffraction (XRD) analysis is a crucial technique for determining the phase, composition, and crystal structure of materials. Figure 2 displays the XRD patterns of pure PVA, Fe_2O_3 nanofillers, and PVA/Fe_2O_3 nanocomposites with varying sizes of Fe_2O_3 nanofillers embedded in the PVA matrix. The XRD pattern of pure PVA, shown in Figure 2(a), features a semi-crystalline peak at $2\theta = 19.770°$, corresponding to the (011) reflection, which indicates the semi-crystalline nature of PVA. This semi-crystallinity is primarily due to strong intermolecular and intramolecular hydrogen bonding among the PVA monomer units. In Figures 2(b-e), the introduction of Fe_2O_3 nanofillers with varying sizes into the PVA matrix results in a slight reduction in the intensity of the PVA peak at $2\theta = 19.770°$. This decrease in intensity can be attributed to several factors, including the dilution effect caused by the dispersion of nanofillers, interference and scattering of X-rays by the nanofillers, and the disruption of the PVA crystalline structure. The dilution effect reduces the concentration of PVA molecules in the peak region, while the nanofillers' scattering and interference further contribute to the intensity reduction by disrupting the formation of well-defined PVA crystallites.

Moreover, the absence of any unwanted peaks in the XRD patterns of the nanocomposites suggests that no new crystalline structures or chemical compounds were formed as a result of the Fe_2O_3 nanofillers' incorporation into the PVA matrix. This observation implies that there were no significant chemical reactions or bonding interactions between the PVA polymer matrix and Fe_2O_3 nanofillers that could lead to the formation of new compounds (Mondal *et al.* 2016; Shahzad *et al* 2024) Additionally, Figure 2(f) illustrates the typical XRD pattern of the Fe_2O_3 nanofillers, which confirms their crystalline nature by displaying sharp diffraction peaks. The XRD spectra of the Fe_2O_3 nanofillers reveal a series of diffraction patterns at 2θ values of 27.168°, 34.234°, 53.586°, 65.579°, and 72.555°, corresponding to the (131), (060), (402), (281), and (135) planes, respectively. These peaks are consistent with the monoclinic structure and match the International Crystallographic Structural Database (ICSD) card No. 98-007-7744. Figure 2 provides a comprehensive view of the XRD patterns for pure PVA, the Fe_2O_3 nanofillers, and the PVA/Fe_2O_3 nanocomposites with varying sizes of Fe_2O_3 nanofillers.

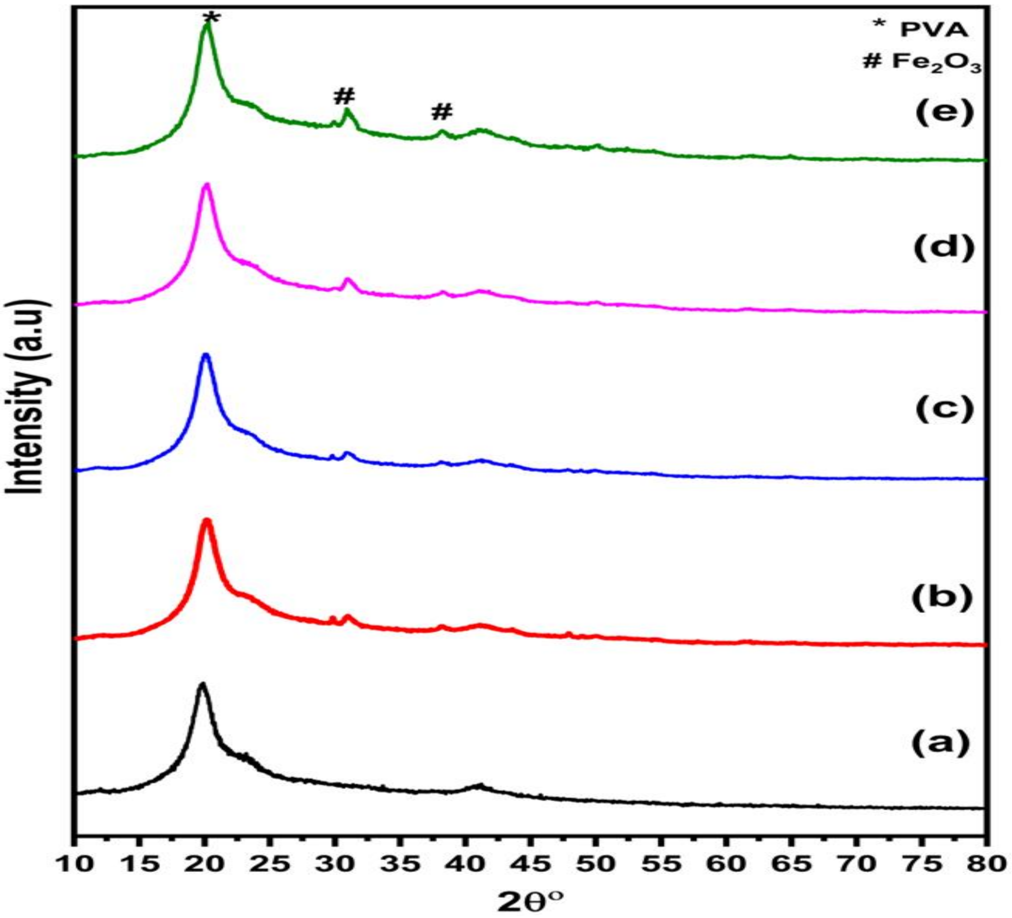

Figure 2: XRD graph of Fe_3O_4/PVA nanocomposites (a) PVA (b) 1.2wt% (c) 2.4wt% (d) 3.6wt% (e) 4.8wt%

Scherer's Method

Scherer's method, commonly referred to as the Scherrer equation or Scherrer's formula, is a well-established technique for estimating the crystallite size in materials based on the broadening of X-ray diffraction (XRD) peaks (Zhang *et al.* 2014).This method is instrumental in providing insights into the average size of crystalline domains within a sample. The Scherrer equation is grounded in the fundamental principles of X-ray diffraction and accounts for the peak broadening that arises due to the finite size of the crystallites. The equation relates the crystallite size (D) to the observed peak broadening (β), the wavelength of the X-rays used (λ), the Bragg angle (θ), and a dimensionless shape factor (K) that depends on the assumed shape of the crystallites (Wu *et al.* 2018). The formula is expressed as:

$$D = \frac{k\lambda}{\beta_{hkl}\cos\theta} \quad (1)$$

Where λ X-ray wavelength, k is the shape factor (usually taken as 0.9) β is the full width at half maximum (FWHM) of the diffraction peaks and θ is the Bragg's angle of reflection (Xing *et al.* 2020). To apply Scherer's method, X-ray diffraction (XRD) measurements were conducted on the Fe_2O_3 nanoparticles. The XRD pattern provided crucial information regarding the positions and intensities of the diffraction peaks, which correspond to the specific crystal planes within the material. Due to the finite size of the crystalline domains, the peaks in the XRD pattern appeared broader, a phenomenon that Scherer's method utilizes to estimate the crystallite size (Deshmukh *et al.*2016). Figure 3 illustrates the application of Scherer's method to Fe_2O_3 nanoparticles synthesized at various sintering temperatures. The figure also includes the respective equations derived from the linear least square method, obtained from the linear regression of the data plots. The crystallite size, as estimated by Scherer's method, was found to be 20.66 nm, 36.39 nm, 34.58 nm, and 38.30 nm for sintering temperatures of 200°C, 300°C, 400°C, and 500°C, respectively. These results demonstrate the influence of sintering temperature on the crystallite size, with a general trend of increasing crystallite size at higher sintering temperatures.

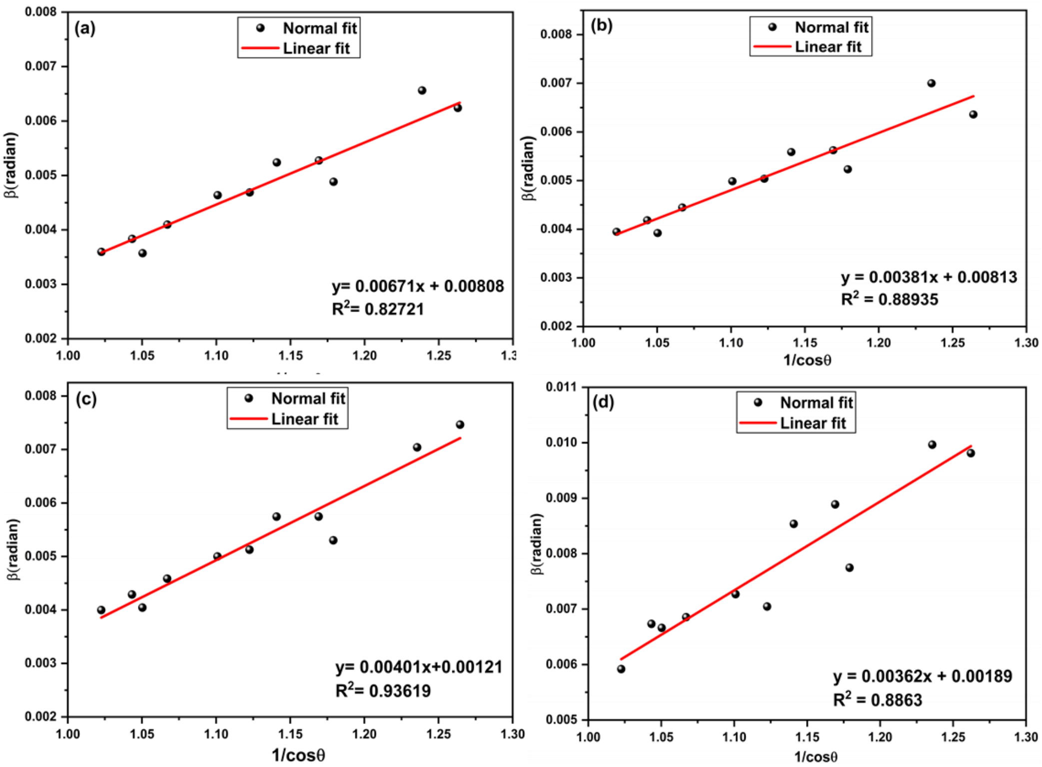

Figure 3: Scherer’s method estimated crystallite size of Fe_2O_3 at different sintering temperatures (a) 200℃ (b) 300℃ (c) 400℃ (d) 500℃

Modified Scherer’s Method (Monshi-Scherrer Method)

The Modified Scherer's Method is an enhanced technique for estimating the crystallite size in materials using X-ray diffraction (XRD) data. Building on the original Scherrer equation, this method incorporates additional factors that influence peak broadening, allowing for a more precise estimation of crystallite size(Augustin *et al.* 2016).The two key corrections introduced in the Modified Scherer's Method are instrumental broadening and strain broadening. Instrumental broadening arises from the inherent limitations of the XRD equipment, such as the finite size of the X-ray beam and the resolution of the detector (Rajesh Kumar and Hymavathi, 2017)To accurately account for this, instrumental broadening is typically determined experimentally by analysing the diffraction pattern of a standard reference material that has a well-known crystallite size and is free from significant strain effects. By using this reference material, the instrumental broadening can be quantified and subsequently corrected for in the crystallite size estimation (Maharaz *et al*. 2018).

Strain broadening, on the other hand, occurs due to lattice strain or microstrain within the crystalline domains. This type of broadening can be caused by lattice defects, non-uniform stress distributions, or other forms of microstrain within the crystal lattice (Akir *et al.* 2016). The Modified Scherer's Method introduces an additional term to the crystallite size equation to account for strain broadening, allowing for a more accurate determination of the crystallite size. The modified equation is expressed as (Maharaz *et al*. 2018):

$$\ln\beta = \ln\left(\frac{K\lambda}{D}\right) + \ln\left(\frac{1}{\cos\theta}\right) \qquad (2)$$

As a result, plotting a graph of lnβ (β in radian) on the y-axis and $\ln\left(\frac{1}{\cos\theta}\right)$ on the x-axis results in a linear plot for all of the selected peaks of the XRD pattern. After establishing the fitted linear plots, the crystallite size (D) can be calculated from the graph's intercept (Muthu and Babu, 2018). Figure 4 depicts the plots of the modified Scherer's method of Fe_2O_3 nanoparticle synthesised at various sintering temperatures, as well as their respective equation of the linear least square method obtained from the linear regression data plots. Equation (3) is employed simply to calculate the crystallite size (D) of Fe_2O_3 nanoparticles using the modified Scherrer’s method (Han *et al*, 2018):

$$\frac{K\lambda}{D} = e^{(\text{intercept})} \qquad (3)$$

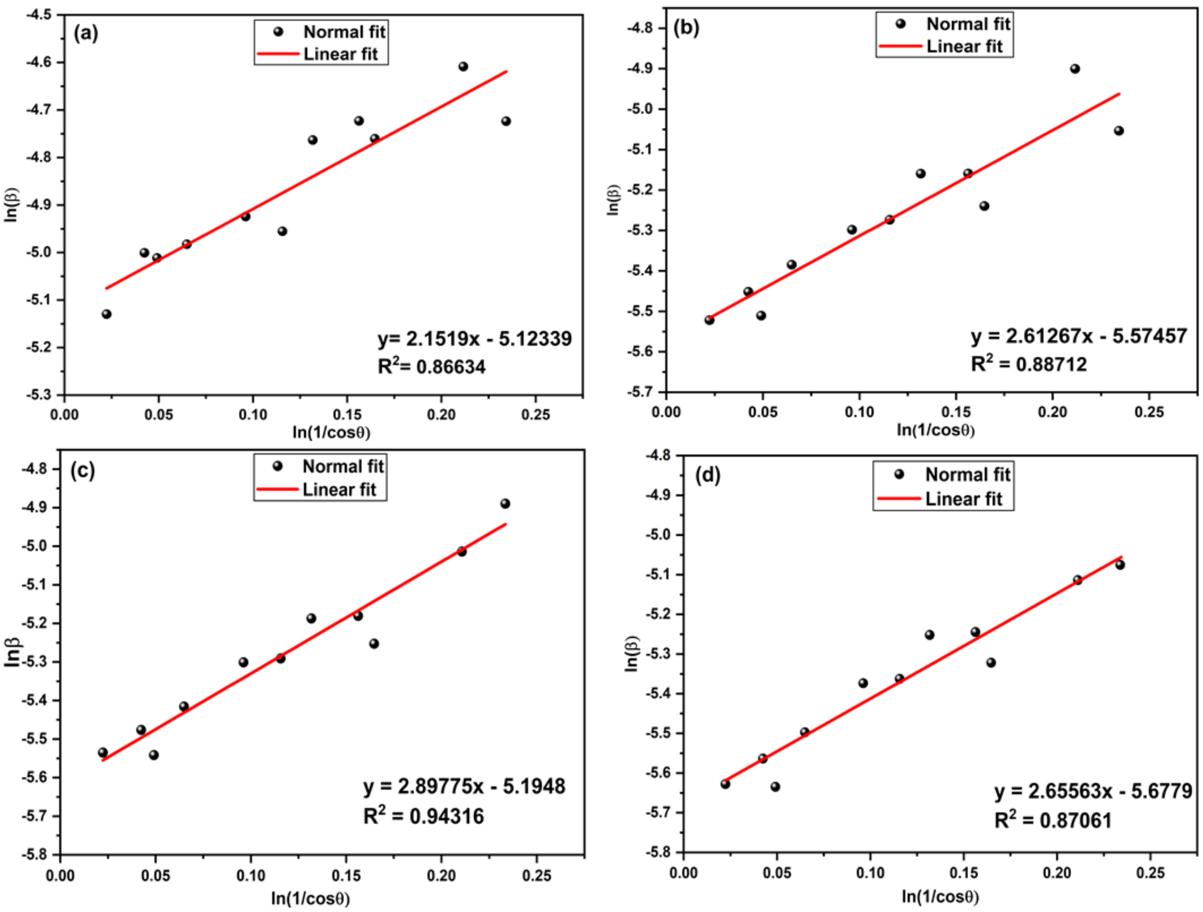

Figure 4: Modified Scherer's method estimated crystallite size of Fe_2O_3 at different sintering temperatures (a) 200℃ (b) 300℃ (c) 400℃ (d) 500℃

Size Strain Plot Method (SSP)

The Size Strain Plot (SSP) method is a commonly employed technique for estimating both the crystallite size and microstrain in a material by analysing X-ray diffraction (XRD) data. This method provides crucial insights into the average size of the crystalline domains and the extent of any lattice distortions or microstrain within the material (Aydın and Abacı, 2017). The SSP method is particularly valuable because it considers the broadening of XRD peaks, which results from several factors, including the finite size of the crystallites and the presence of lattice strain or distortions. The method quantifies peak broadening by analysing the XRD pattern, allowing for the determination of both crystallite size and microstrain (Ichi *et al.* 2017). It is based on the assumption of an isotropic strain distribution within the crystalline domains, meaning that the strain is uniform in all directions. Accurate determination of these parameters requires precise measurement and careful analysis of the XRD peaks, taking into account factors such as instrumental broadening and any other influences that may affect peak shape. As a result, the total peak broadening in the size-strain plot method (SSP) can be calculated using the formula as follows (Singh *et al.* 2018):

$$\beta_{hkl} = \beta_L + \beta_G \quad (4)$$

where β_L and β_G are Lorentzian and Gaussian Peak broadening. The SSP method separates the contributions of size and strain effects on the broadening of X-ray diffraction peaks. By considering both factors separately, it becomes easier to analyse and quantify the effects of isotropic enlargement (Kombaiah *et al.* 2017). Furthermore, the size strain plot (SSP) method consistently yields superior results when analysing isotropic enlargement. This is attributed to its enhanced applicability to low angle reflections, where higher accuracy and precision are achieved compared to higher angles. The quality of X-ray diffraction (XRD) data tends to decrease at higher angles, leading to significant peak overlapping. In contrast, the lower diffraction angles provide clearer and more reliable information. The SSP calculation is performed using the following equation express as (Garba *et al* 2020):

$$(d_{hkl}\beta_{hkl}\cos\theta)^2 = \frac{K\lambda}{D}\left(d_{hkl}^2\beta_{hkl}\cos\theta\right) + \frac{\varepsilon^2}{4} \quad (5)$$

where d_{hkl} is lattice separation between the lattice plane (hkl) of the hexagonal crystal structure. The lattice separation between the diffraction planes (hkl) can be calculated using the equation express as: The lattice separation between the diffraction planes (hkl) can be calculated using the equation express as (Hou *et al* 2018):

$$\frac{1}{d_{hkl}^2} = \frac{4}{3}\left(\frac{h^2 + hk + k^2}{a^2}\right) + \left(\frac{l^2}{c^2}\right) \quad (6)$$

$$d_{hkl}^2 = \left(\frac{a^2}{h^2+k^2+l^2}\right) \quad (7)$$

Therefore, a plot of $(d_{hkl}\beta_{hkl}\cos\theta)^2$ on y-axis and $\left(d_{hkl}^2\beta_{hkl}\cos\theta\right)$ on the X-axis is drawn as shown in Figure 5. Using the slope and intercept from the linearly fitted data, the mean crystallite size and the intrinsic strain of Fe_2O_3 NPs is obtained. As shown in Table 2, the estimated crystallite size and microstrain at various sintering temperature of 200, 300, 400, and 500 were found to be 23.28, 25.14, 38.27, and 41.12 nm, and 2.79×10^{-8}, 2.87×10^{-8}, 82.59×10^{-8}, and 1.19×10^{-7} respectively.

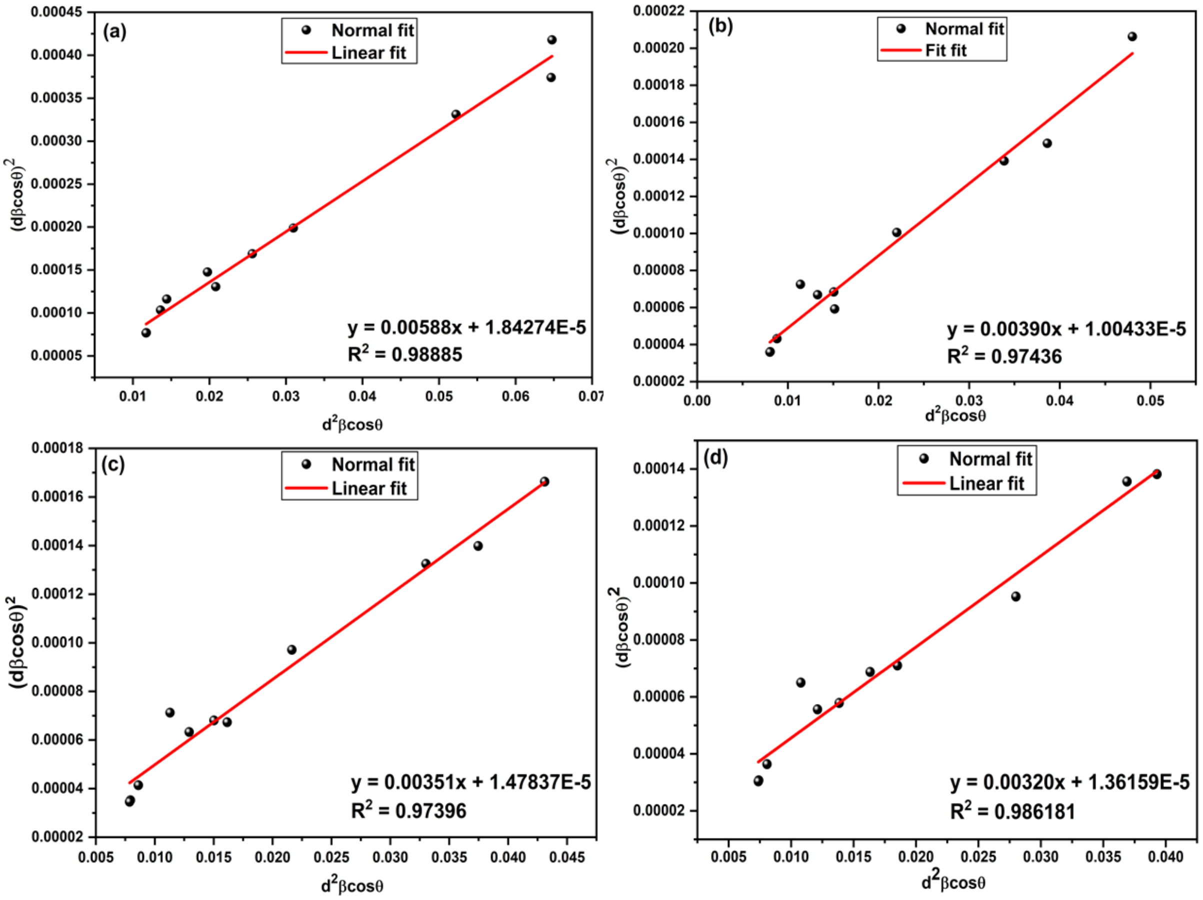

Figure 5: Size- Strain Plot method estimated crystallite size of Fe_2O_3 at different sintering temperatures (a) 200°C (b) 300°C (c) 400°C (d) 500°C

Halder-Wagner Method

The Halder-Wagner method is a widely utilized technique for estimating the crystallite size and microstrain in nanoparticles using X-ray diffraction (XRD) data. This method establishes a relationship between crystallite size and microstrain, which is mathematically expressed by the following equation (Ghosh *et al*. 2016):

$$\beta_{\mathrm{hkl}}^2 = \beta_L \beta_{\mathrm{hkl}} + \beta_G^2 \qquad (8)$$

where β is the FWHM of the diffraction peak, θ is the Bragg angle, λ is the wavelength of the X-ray radiation, D is the crystallite size, and ε is the microstrain. The Halder-Wagner method assumes that the spreading of the peak is a symmetric Voigt function, which means that the crystallite size and microstrain are estimated simultaneously (Shinde *et al.*2017). In contrast, the Williamson-Hall method considers the effect of strain on the XRD peak broadening and can be used for the estimation of the intrinsic strain separated from the crystallite size. The Halder-Wagner method assumes that the crystallites are spherical and that the XRD peak profile is described by a linear combination of Lorentz and Gaussian functions. According to the Halder-Wagner method, the following formula describes the relationship between crystallite size and lattice strain (Das *et al*. 2018):

$$\left(\frac{\beta^*_{\mathrm{hkl}}}{d^*_{\mathrm{hkl}}}\right)^2 = \frac{1}{D}\cdot\frac{\beta^*_{\mathrm{hkl}}}{{d^*_{\mathrm{hkl}}}^2} + \left(\frac{\varepsilon}{2}\right)^2 \qquad (9)$$

where $d^*_{\mathrm{hkl}} = 2d_{\mathrm{hkl}}\cdot\frac{\sin\theta}{\lambda}$. A linear plot will be obtained by plotting a graph of $\left(\frac{\beta^*_{\mathrm{hkl}}}{d^*_{\mathrm{hkl}}}\right)^2$ as the Y-axis and $\frac{\beta^*_{\mathrm{hkl}}}{{d^*_{\mathrm{hkl}}}^2}$ as the x-axis for every XRD pattern. Figure 6 illustrates the Halder-Wagner plots along with the linear least square equations derived from the linear regression of the plotted data. The average crystallite size is determined from the slope of the linear plot, while the intrinsic strain of the Fe_2O_3 nanoparticles is derived from the intercept. According to the graph, the crystallite sizes at sintering temperatures of 200°C, 300°C, 400°C, and 500°C are estimated to be 23.28 nm, 25.14 nm, 38.27 nm, and 41.12 nm, respectively. The corresponding microstrain values are calculated to be 2.79×10^{-8}, 2.87×10^{-8}, 82.59×10^{-8}, and 1.19×10^{-7}. The results obtained from the Halder-Wagner method show strong agreement with those derived from the Scherer and Monshi-Scherer methods, indicating the consistency and reliability of the crystallite size and microstrain estimates. This agreement validates the robustness of the Halder-Wagner method in analysing the microstructural parameters of the nanoparticles. These parameters, including the crystallite size and microstrain for all samples, are summarized in Table 1, providing a detailed overview of the structural characteristics of Fe_2O_3 nanoparticle at different sintering temperatures.

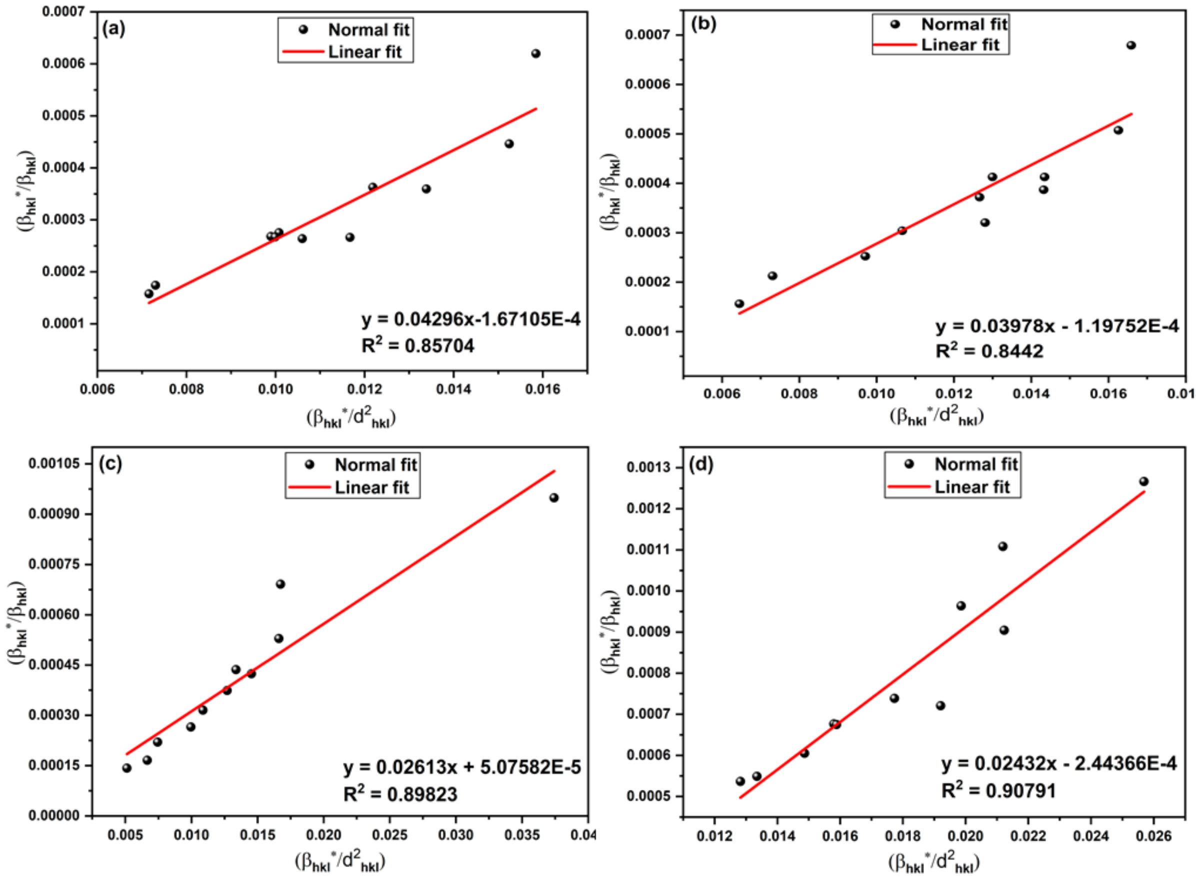

Figure 6: Halder Wagner method estimated crystallite size of Fe_2O_3 at different sintering temperatures (a) 200℃ (b) 300℃ (c) 400℃ (d) 500℃

Table 1: Crystallographic parameter of Fe_2O_3 estimated using SM, MSM, SSP, and HWM at different sintering temperature

S/N	Sample Designation	Scherer's Method (SM)		Monshi-Scherrer Method (MSM)		Size Strain Plot Method (SSP)		Halder-Wagner Method (HWM)	
		Size (nm)	Strain ($\times 10^{-3}$)	Size (nm)	Strain ($\times 10^{-3}$)	Size (nm)	Strain ($\times 10^{-3}$)	Size (nm)	Strain ($\times 10^{-3}$)
1	Fe_2O_3@200℃	20.66	2.35	23.26	2.15	23.58	8.56	23.28	2.79
2	Fe_2O_3@300℃	34.58	2.26	36.58	2.61	35.55	6.34	25.14	2.87
3	Fe_2O_3@400℃	36.39	2.22	38.30	2.89	39.50	7.69	38.27	2.57
4	Fe_2O_3@500℃	38.30	2.18	40.54	2.65	43.32	7.38	41.12	1.20

Williamson-Hall Method (WHM)

The Scherrer equation only accounts for the effect of crystallite size on the broadening of X-ray diffraction (XRD) peaks and does not consider intrinsic strain that may develop in nanocrystals due to factors such as point defects, grain boundaries, triple junctions, and stacking faults. As a result, it cannot estimate intrinsic strain. In contrast, the Williamson-Hall method takes into account the broadening caused by both crystallite size and strain, allowing for the estimation of both crystal size and intrinsic strain (Lala *et al.* 2017). Unlike the Scherrer equation, which follows a 1/cosθ dependency, the Williamson-Hall method uses a tanθ dependency to account for strain-induced broadening, effectively separating the contributions from crystallite size and microstrain. The Halder-Wagner method is another technique that considers the effect of strain on XRD peak broadening. It is often considered more suitable than the Williamson-Hall method for estimating lattice strain and crystallite size (Ma *et al.* 2017). The Halder-Wagner method assumes that the broadening of the XRD peaks can be described by a symmetric Voigt function, which allows for the simultaneous estimation of crystallite size and microstrain. The accuracy of these methods depends on several factors, including the quality of the XRD pattern, the shape factor, and the assumptions made about the crystal structure. The total broadening observed in the XRD peaks is a result of the combined influence of crystallite size and intrinsic strain on the nanocrystals. This total broadening can be described by the following expression (Jeevanandam *et al.* 2018):

$$\beta_{hkl} = (\beta_{size} - \beta_{strain}) \quad (10)$$

Here, β_{size} and β_{Strain} represent the XRD peak broadening (full width at half maximum, FWHM) due to the crystallite size and intrinsic strain of the nanoparticle, respectively. In this research, modified Williamson-Hall (W-H) methods were utilized, specifically incorporating three models: Uniform Deformation Model (UDM), Uniform Stress Deformation Model (USDM), and Uniform Deformation Energy Density Model (UDEDM). These modified W-H methods were applied to estimate the microstrain and crystallite size of nanoparticles using X-ray diffraction (XRD) data. The application of these models enabled a detailed analysis, successfully facilitating the determination of energy density, stress, and strain values within the nanoparticles (Zhang *et al.* 2016). By using these approaches, the study provided a comprehensive understanding of the mechanical properties of the nanoparticles, beyond simple crystallite size estimation, offering valuable insights into the effects of strain and stress on the structural properties of the materials (Giribabu et al. 2013).

Uniform Deformation Model (UDM)

The Uniform Deformation Model (UDM) is an extension of the Williamson-Hall Method for estimating crystallite size and lattice strain in materials based on x-ray diffraction (XRD) data. It provides a more comprehensive analysis by considering both size and strain effects on the XRD peak broadening. The UDM assumes that the crystallite size and the lattice strain contribute independently to the XRD peak broadening. It considers the effects of both microstructural imperfections and lattice distortions within the crystalline domains (Wu *et al*. 2016). The size broadening arises from the finite size of the crystalline domains, while the strain broadening is caused by lattice distortions or microstrain within the material. The broadening of X-ray diffraction (XRD) peaks is influenced by intrinsic strain, which causes line broadening. The broadening of peaks induced by the strain can be mathematically expressed as (Chen *et al*. 2017) :

$$\beta_{\text{strain}} = 4\varepsilon\sin\theta \qquad (11)$$

Therefore, the total broadening of X-ray diffraction (XRD) peaks, arising from the combined influences of size and strain effects across all the diffraction planes (hkl), can be mathematically expressed as:

$$\beta_{\text{hkl}} = (\beta_{\text{size}} - \beta_{\text{strain}}) \qquad (12)$$

where β_{hkl} represents the Full Width at Half Maximum (FWHM) of the diffraction planes (hkl) for either all or specific selected peaks in the x-ray diffraction (XRD) spectra, while β_{size}can be express as:

$$\beta_{\text{size}} = \frac{k\lambda}{D}.\frac{1}{\cos\theta}, \qquad (13)$$

and

$$\beta_{\text{strain}} = 4\varepsilon\sin\theta. \qquad (14)$$

The formula for the uniform deformation model can be expressed as follows:

$$\beta_{\text{hkl}} = \frac{k\lambda}{D}.\frac{1}{\cos\theta} + 4\varepsilon\sin\theta \qquad (15)$$

Rearranging equation (00) yields:

$$\beta_{\text{hkl}}\cos\theta = \frac{k\lambda}{D} + 4\varepsilon\sin\theta \qquad (16)$$

Equation (16) represents a linear equation known as the uniform deformation model (UDM). Figure 7 displays the plots obtained from equation (16). These plots correspond to the major diffraction peaks of Fe_2O_3 nanoparticles. The slope and intercept of the linearly fitted graph provide information about the intrinsic strain and the average crystallite size of Fe_2O_3 nanoparticles synthesized at different sintering temperatures. The presence of lattice strain is primarily attributed to the expansion or contraction of the crystal lattices in nanocrystals, resulting from the size confinement effect (Lee *et al.* 2013). Consequently, the atomic arrangement in nanocrystals slightly differs from that of their bulk counterparts. Moreover, size confinement leads to the creation of defects within the lattice structure, further contributing to lattice strain (Singh et al. 2018). Figure 6 depicts the UDM plots of Fe_2O_3 nanoparticles synthesized at different irradiation times.

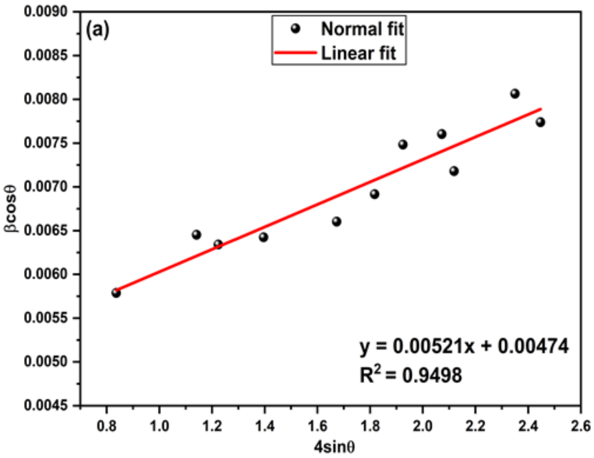

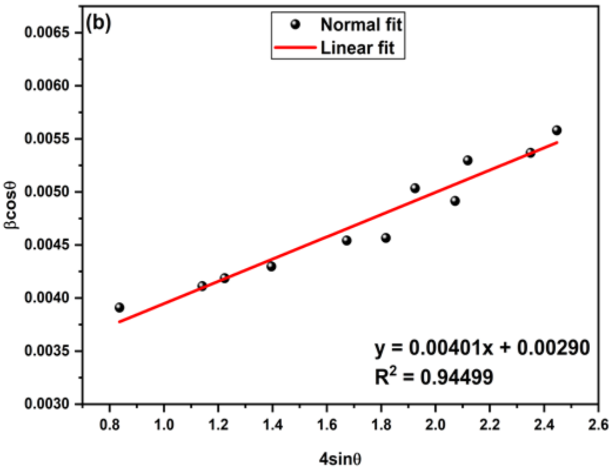

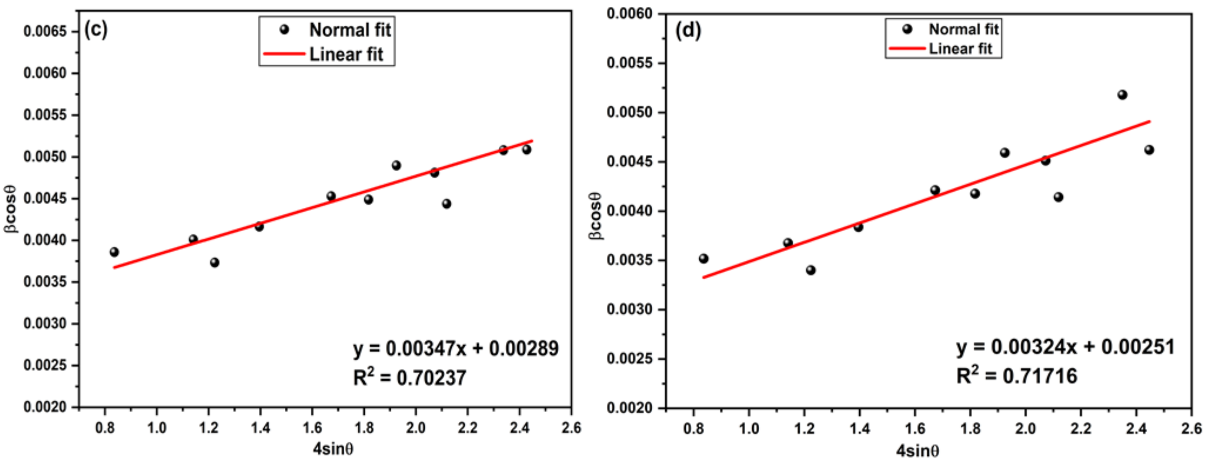

Figure 7: Uniform deformation Model (UDM) method estimated crystallite size of Fe_2O_3 at different sintering temperatures (a) 200℃ (b) 300℃ (c) 400℃ (d) 500℃

X-ray Dispersive Spectroscopy (EDX)

Energy-Dispersive X-ray (EDX) analysis is a crucial technique used to validate the elemental composition of synthesized nanoparticles. In this study, EDX analysis was performed to confirm the composition of the Fe_2O_3 nanoparticles, with a particular focus on those sintered at 300°C. The results, presented in Figure 8, reveal the chemical composition of the synthesized nanoparticles. The EDX spectra clearly indicate the presence of oxygen (O) and iron (Fe) elements, confirming that the nanoparticles are composed of Fe_2O_3. Importantly, no signals from other elements were detected, underscoring the high purity of the synthesized Fe_2O_3 nanoparticles. The observed percentages of Fe and O closely match the amounts used in the precursor materials, providing strong evidence that the combustion process did not result in significant elemental loss. This indicates the efficiency and effectiveness of the synthesis method in preserving the desired elemental composition of the Fe_2O_3 nanoparticles. Additionally, a minor peak corresponding to carbon (C) was detected in the EDX spectra, which is attributed to the presence of electric latex in the EDX sample holder (Chen and Chuang, 2013). These findings are consistent with previous studies that have employed EDX analysis to assess the composition of Fe_2O_3 nanoparticles, further validating the results of this research.

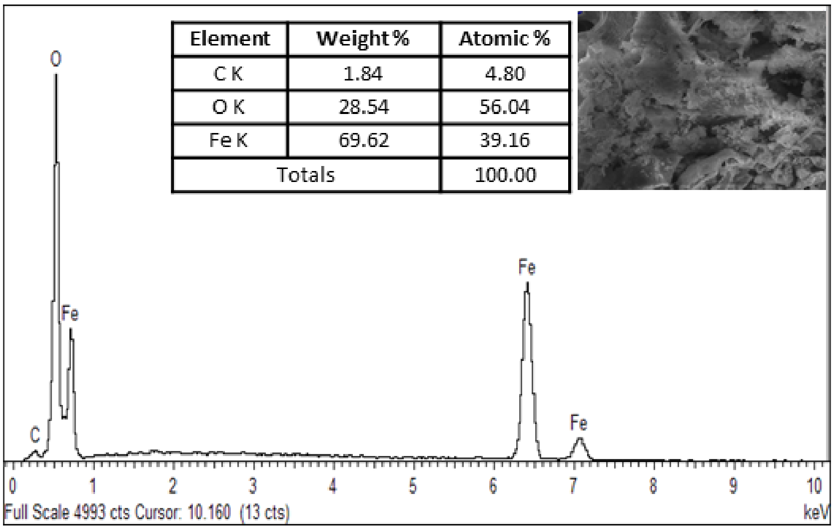

Element	Weight%	Atomic%
C K	1.84	4.80
O K	28.54	56.04
Fe K	69.62	39.16
Totals		100.00

Figure 8: EDX spectra of Fe_2O_3 nanoparticles sintered at 300^0C

Analysis of Magnetic Properties of Hematite (Fe_2O_3) Nanoparticles

The magnetic characteristics of hematite (Fe_2O_3) nanoparticles were thoroughly investigated at room temperature using a Vibrating Sample Magnetometer (VSM). The experimental setup involved applying a magnetic field that ranged from -15,000 to 15,000 Oe, allowing for the analysis of magnetic hysteresis loops, as illustrated in Figure 9. These loops provide crucial insights into the relationship between magnetization and the applied magnetic field, offering a clear visualization of the magnetic behaviour of the hematite nanoparticles under varying magnetic field strengths (Saini et al. 2018). The data revealed that the synthesized nanoparticles possess a saturation magnetization (Ms) value of 4.0 emu/g, which was measured at an applied field of approximately -15,000 Oe. Saturation magnetization is a key parameter representing the maximum magnetic moment that can be achieved in a material, and the Ms value of 4.0 emu/g indicates a substantial level of magnetization in the hematite nanoparticles (Gurusiddesh et al. 2018).

Further analysis of the hysteresis loop suggests that the synthesized hematite nanoparticles exhibit superparamagnetic behaviour. This is evidenced by the absence of coercivity and remanence, indicating that the nanoparticles do not retain any permanent magnetic moment once the external magnetic field is removed (Chhetri *et al.* 2017). Such behaviour is characteristic of superparamagnetic materials, which display magnetic properties only in the presence of an external magnetic field and do not exhibit residual magnetization. The saturation magnetization value of 4.0 emu/g obtained in this study aligns with values reported in previous studies (Pasha et al. 2017). The consistency of these findings across multiple studies enhances the credibility and validity of the results, further confirming the superparamagnetic properties of the hematite nanoparticles synthesized in this research.

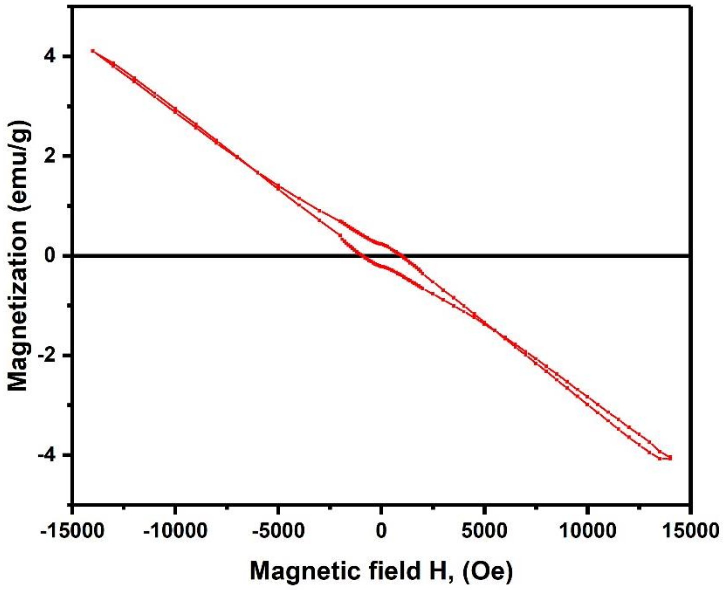

Figure 9: Magnetization curve for Fe_2O_3 nanoparticles sintered at 400°C

Analysis of Hematite (Fe_2O_3) Particle Size using Field Emission Scanning Electron Microscopy (FESEM)

Figure 10 presents the Field Emission Scanning Electron Microscopy (FESEM) images and the corresponding size distribution histogram of Fe_2O_3 nanoparticles sintered at various temperatures. The average particle size was estimated to be [insert specific sizes here] corresponding to sintering temperatures of 200°C, 300°C, 400°C, and 500°C, respectively. As clearly observed in Figure 10, there is a notable increase in average particle size with the rise in sintering temperature. This trend can be attributed to several underlying processes that occur during the sintering of nanoparticles, such as surface diffusion, coalescence, and grain boundary migration (Karteri *et al.* 2017). At higher sintering temperatures, the thermal energy available to the nanoparticles increases, enhancing surface diffusion and the movement of atoms or molecules across the particle surfaces. As the thermal energy rises, the surface atoms or molecules become more mobile, promoting their migration and leading to the coalescence of adjacent particles. This coalescence results in the agglomeration and merging of nanoparticles, which in turn causes an increase in the average particle size (Al-Saleh *et al*. 2015).

Additionally, grain boundary migration becomes more significant at elevated temperatures. Grain boundaries, which are interfaces between adjacent crystalline grains, migrate during the sintering process, facilitating the rearrangement and coalescence of nanoparticles. This migration contributes further to the growth of particle size (Song *et al.*2014). It is important to recognize that the extent of particle growth during sintering is influenced by various factors, including sintering time, heating rate, and the composition of the nanoparticles. While higher sintering temperatures generally promote particle growth, the specific behaviour can vary depending on the experimental conditions and the system under study (Alghunaim,2019). Therefore, careful control of the sintering temperature is crucial to achieve the desired particle size and to maintain the optimal properties of the synthesized nanoparticles.

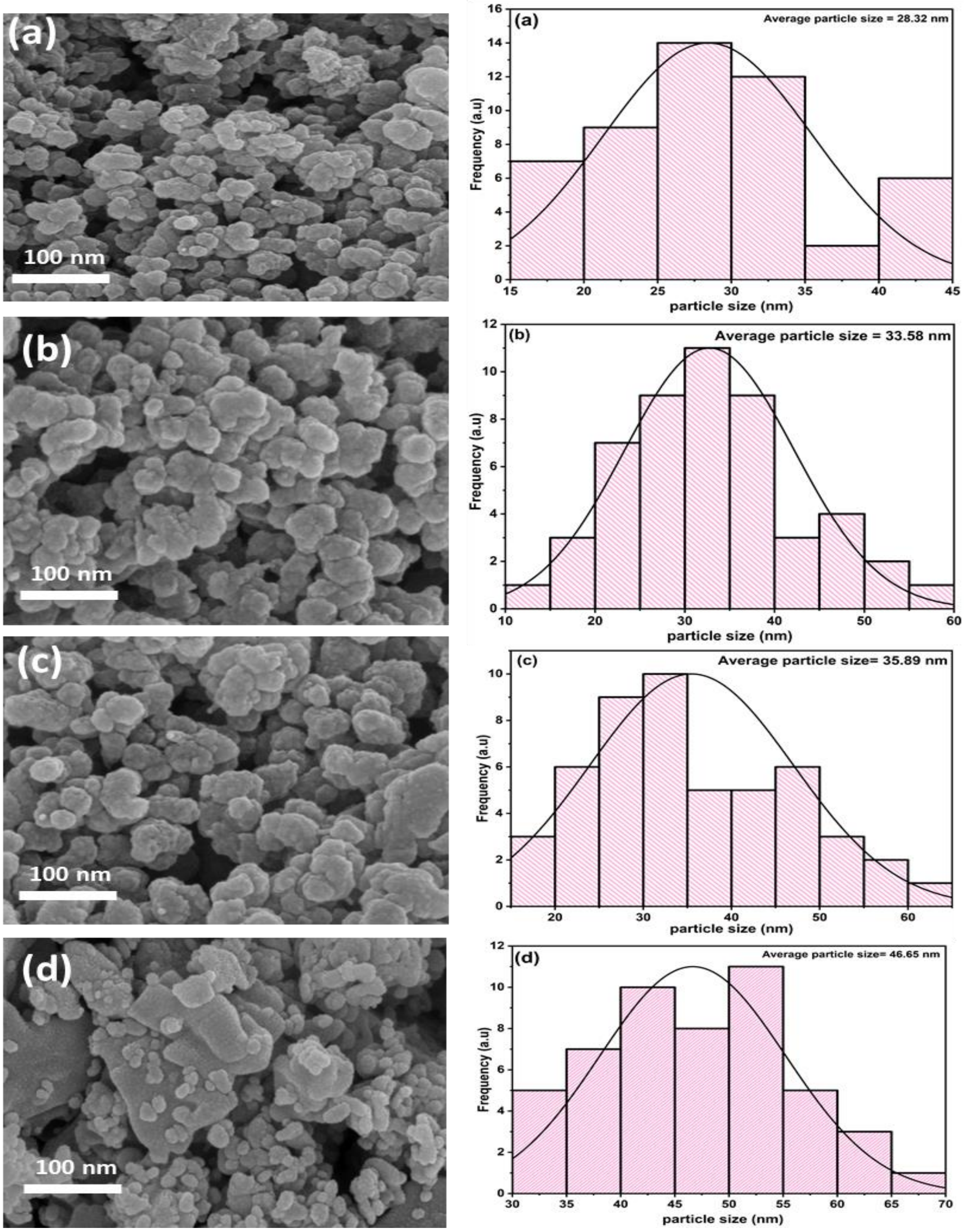

Figure 10: FESEM images and size distribution histogram of Fe_2O_3 at different sintering temperatures (a) 200℃ (b) 300℃ (c) 400℃ (d) 500℃

Total Electromagnetic Interference (EMI) Shielding Application

Reflection Loss (SE_R)

The graph in Figure 11 illustrates the reflection loss (SE_R) of Fe_2O_3/PVA nanocomposites across a frequency range of 8 to 12 GHz for varying filler loadings. The pure PVA sample exhibits the lowest reflection loss, with SE_R values consistently below 0.5 dB, indicating minimal electromagnetic wave absorption due to the absence of conductive or magnetic particles. As the Fe_2O_3filler loading increases, the reflection loss significantly rises. At 1.2 wt% Fe_2O_3, the SE_R increases to approximately 1dB, suggesting that the magnetic properties of Fe_2O_3 nanoparticles introduce magnetic loss mechanisms that enhance electromagnetic absorption. With a further increase to 2.4 wt% Fe_2O_3, the reflection loss escalates to around 2.5 dB, as the higher concentration of Fe_2O_3 improves impedance matching and intensifies magnetic losses through mechanisms such as magnetic hysteresis, domain wall resonance, and eddy current losses (Yu *et al.* 2012). The highest filler loading of 3.6 wt% Fe_2O_3 results in the most substantial reflection loss, with SE_R values peaking around 3.5 dB. This significant increase in reflection loss indicates that the nanocomposite's ability to absorb electromagnetic waves is maximized at this concentration. The enhanced absorption is likely due to the optimal balance between the dielectric properties of the PVA matrix and the magnetic properties of the Fe_2O_3 particles, which together contribute to improved impedance matching and energy dissipation through both magnetic and dielectric loss mechanisms (Muzaffar et al. 2019). This observed trend highlights the potential of Fe_2O_3/PVA nanocomposites for applications in electromagnetic interference (EMI) shielding and microwave absorption. The increased filler content significantly enhances the material's effectiveness by improving impedance matching and enabling more efficient energy dissipation, as supported by previous studies (Al-Ghamdi et al. 2015).

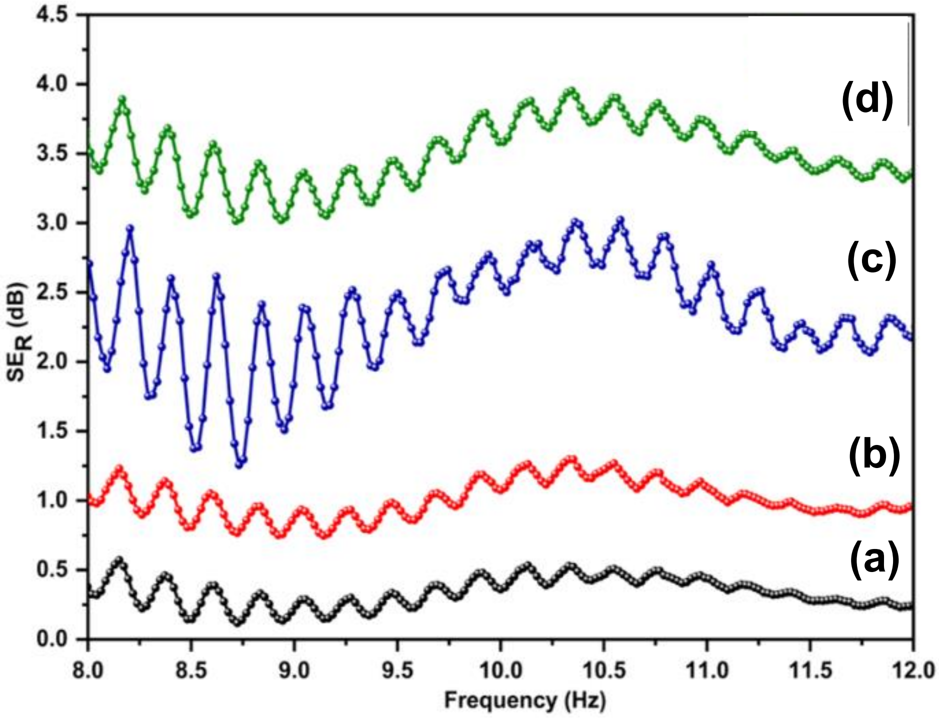

Figure 11: Reflection loss of Fe_3O_4/PVA nanocomposites at different filler loading (a) PVA (b) 1.2wt% (c) 2.4wt% (d) 3.6wt% (e) 4.8wt%

Absorption Loss (SE_A)

The graph in Figure 12 illustrates the absorption loss (SEA) of Fe_2O_3/PVA nanocomposites as a function of frequency for Fe_2O_3 at different weight percentage (wt%) in polyvinyl Alcohol (PVA) polymer matrix. The pure PVA sample (neat PVA) exhibits the lowest absorption loss, with SEA values ranging between 5 and 10 dB across the 8 to 12 GHz frequency spectrum. This indicates that PVA alone has a limited capacity to absorb electromagnetic waves due to its lack of magnetic or conductive components, which are essential for significant electromagnetic attenuation (Al-Ghamdi et al. 2015). Conversely, the introduction of 1.2 wt% Fe_2O_3 into the PVA matrix raises the SE_A values to approximately 10 to 15 dB, a boost attributed to the presence of magnetic Fe_2O_3 nanoparticles that enhance energy dissipation through mechanisms such as magnetic hysteresis and eddy current losses. Increasing the Fe_2O_3 content further to 2.4 wt% results in SEA values of around 15 to 20 dB, signifying improved electromagnetic absorption. This improvement is due to the higher concentration of magnetic particles, which enhances the composite's impedance matching and increases the efficiency of both magnetic and dielectric loss mechanisms (Lin Yao *et al*. 2017). The highest filler loading of 3.6 wt% Fe_2O_3 achieves the maximum SEA values, ranging from 20 to 25 dB. This trend underscores the synergistic effect of the magnetic Fe_2O_3 particles and the dielectric PVA matrix, which together optimize impedance matching and maximize energy dissipation through increased magnetic and dielectric losses (Zhang et al. 2016).

The observed increase in SE_A with higher Fe_2O_3 content demonstrates the potential of $Fe_2O/_3$PVA nanocomposites for applications requiring effective electromagnetic interference (EMI) shielding and microwave absorption. The magnetic Fe_2O_3 nanoparticles significantly enhance the material's ability to absorb electromagnetic waves, while the PVA matrix provides a dielectric environment that aids in impedance matching, thereby reducing reflection and increasing absorption (Tchouank et al. 2020). This combination of properties makes $Fe_2O/_3$PVA nanocomposites a promising material for advanced EMI shielding applications, as supported by previous research.

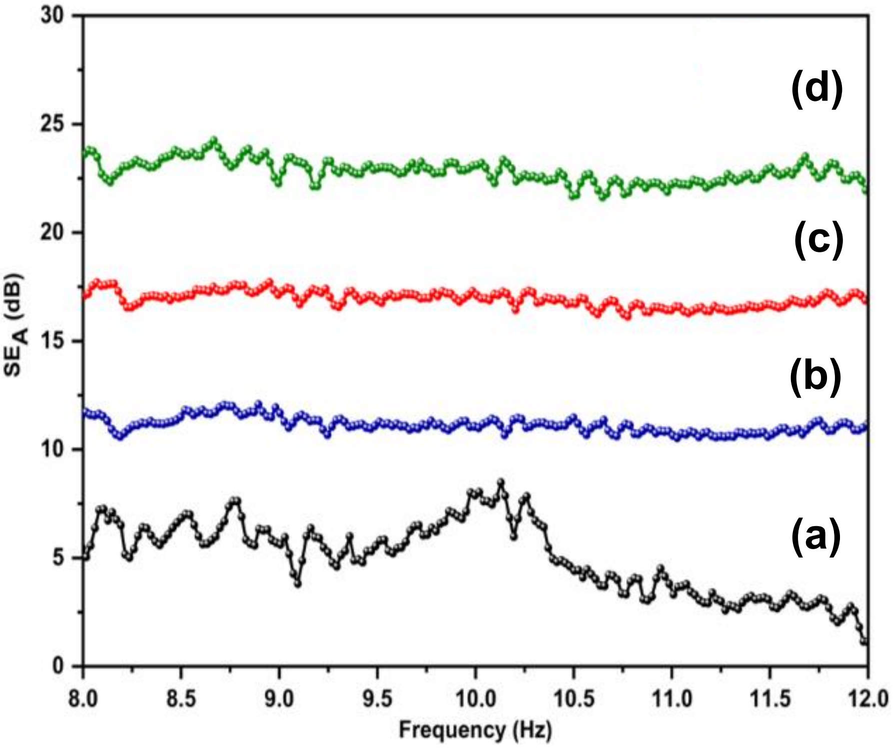

Figure 12: Absorption loss of Fe_3O_4/PVA nanocomposites at different filler loading (a) PVA (b) 1.2wt% (c) 2.4wt% (d) 3.6wt% (e) 4.8wt%

Total Electromagnetic Interference Shielding Effectiveness (EMI SE)

Figure 13 illustrates the total shielding effectiveness (SET) of Fe_2O_3/PVA nanocomposites over a frequency range of 8.0 to 12.0 GHz. The SE_T, measured in decibels (dB), is plotted on the y-axis, while the frequency (Hz) is shown on the x-axis. The graph features four curves, each representing a different Fe_2O_3filler loading within the PVA matrix. The results reveal a positive correlation between the Fe_2O_3filler loading and the shielding effectiveness. The pure PVA sample (neat PVA) displays the lowest SE_T, with an average value of approximately 5 dB across the entire frequency range, indicating minimal electromagnetic shielding capability due to the absence of magnetic or conductive fillers. Upon introducing 1.2 wt% Fe_2O_3 filler, the SE_T increases to an average of 10 dB, demonstrating an enhanced shielding effectiveness. A further increase in Fe_2O_3 content to 2.4 wt% results in a more pronounced improvement, with SE_T values averaging around 20 dB. The highest SE_T is observed for the 3.6 wt% Fe_2O_3 loading, consistently reaching an average value of 25 dB. These findings align with previous research, which has demonstrated the effectiveness of incorporating magnetic nanoparticles into polymer composites to enhance their electromagnetic shielding properties. The improvement in SE_T with increased Fe_2O_3 filler content can be attributed to the enhanced conductivity and magnetic properties provided by the Fe_2O_3 nanoparticles (Bora, et al. 2017). This trend strongly suggests that Fe_2O_3/PVA nanocomposites are promising materials for applications requiring effective electromagnetic interference (EMI) shielding, as the increased filler content significantly boosts the material's ability to attenuate electromagnetic waves.

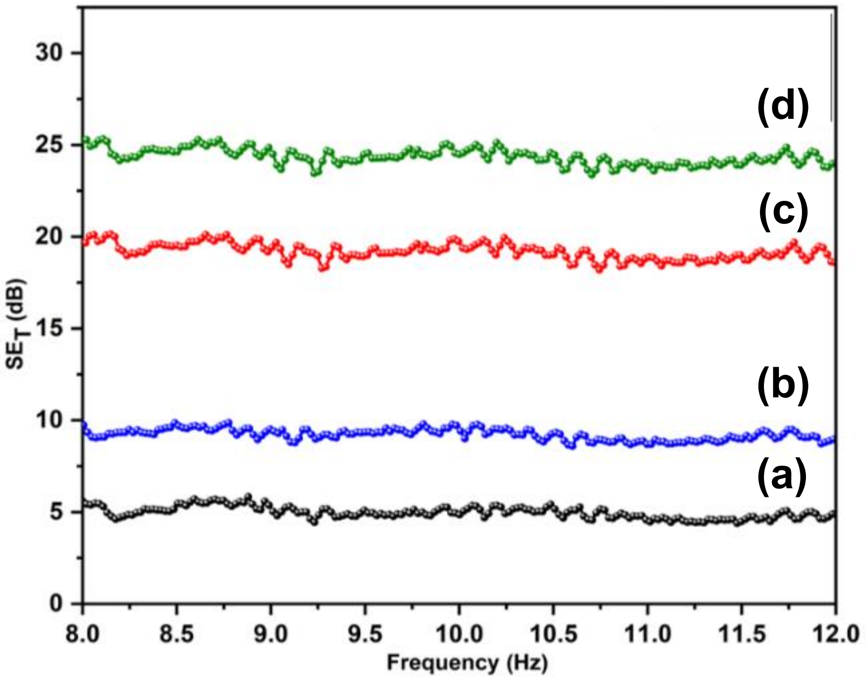

Figure 13: Total shielding effectiveness of Fe_3O_4/PVA nanocomposites at different filler loading (a) PVA (b) 1.2wt% (c) 2.4wt% (d) 3.6wt% (e) 4.8wt%

CONCLUSION

This research successfully synthesized hematite (Fe_2O_3) nanoparticles and investigated the influence of sintering temperature on their structural, magnetic, and electromagnetic interference (EMI) shielding properties. The study confirmed that increasing sintering temperature leads to a consistent growth in crystallite size, as validated by various X-ray diffraction (XRD) techniques and Transmission Electron Microscopy (TEM) analysis. The nanoparticles exhibited superparamagnetic behaviour, with a saturation magnetization of 4.0 emu/g, indicating their strong potential for EMI shielding applications. Additionally, the Fe_2O_3/PVA nanocomposite films showed a significant enhancement in EMI shielding effectiveness, with higher Fe_2O_3 content notably improving both reflection and absorption losses. These findings highlight the critical importance of optimizing sintering temperature to tailor the properties of hematite nanoparticles for advanced technological applications in EMI shielding. The consistent results across different analytical methods further validate the robustness of the synthesis process, making these nanoparticles promising candidates for applications that demand effective electromagnetic interference shielding.

ACKNOWLEDGEMENTS

The authors would like to express their sincere gratitude to the Tertiary Education Trust Fund (TETFund) and Sule Lamido University, Kafin Hausa, Jigawa State, Nigeria, for their generous support and funding, which have been crucial in facilitating the successful completion of this research. Their unwavering commitment to advancing scientific research and innovation has played a pivotal role in enabling the exploration and discoveries presented in this study. We deeply appreciate their dedication to academic excellence and their invaluable contribution to the advancement of knowledge in our community and beyond.

REFERENCES

Akir, A. Barras, Y. Coffinier, M. Bououdina, R. Boukherroub, and A. D. Omrani, (2016) Eco-friendly synthesis of ZnO nanoparticles with different morphologies and their visible light photocatalytic performance for the degradation of Rhodamine B," *Ceram Int*, 42 (8): 10259–10265

Al-Ghamdi, A. A. O. A. Al-Hartomy, F. El-Tantawy, and F. Yakuphanoglu, (2015) Novel polyvinyl alcohol/silver hybrid nanocomposites for high performance electromagnetic wave shielding effectiveness, *Microsystem Technologies*, 21(4): 859–868

Alghunaim, N. S. (2019) Effect of CuO nanofiller on the spectroscopic properties, dielectric permittivity and dielectric modulus of CMC/PVP nanocomposites, *Journal of Materials Research and Technology*, 8(4): 3596–3602

Al-Saleh, M. H. (2015) Influence of conductive network structure on the EMI shielding and electrical percolation of carbon nanotube/polymer nanocomposites, *Synth Met*, 205: 78–84

Augustin, A. K. Rajendra Udupa, and K. Udaya Bhat, (2016) Crystallite size measurement and micro-strain analysis of electrodeposited copper thin film using Williamson-Hall method," *AIP Conf Proc*, vol. 1728

Aydın Z. Y. and S. Abacı, (2017) Synthesis and characterization of Cu3Se2 nanofilms by an underpotential deposition based electrochemical codeposition technique," *Solid State Sci*, 74: 74–87

Bora, P. J. K. J. Vinoy, P. C. Ramamurthy, Kishore, and G. Madras, (2017) Electromagnetic interference shielding effectiveness of polyaniline-nickel oxide coated cenosphere composite film, *Composites Communications*, 4: 37–42

Chen, L. C. Z. L. Tseng, S. Y. Chen, and S. Yang, (2017) An ultrasonic synthesis method for high-luminance perovskite quantum dots," *Ceram Int*, vol. 43 (17) 16032–16035

Chen L. J. and Y. J. Chuang, (2013) Diethylenetriamine assisted synthesis and characterization of stannite quaternary semiconductor Cu2ZnSnSe4 nanorods by self-assembly, *J Cryst Growth*, 376: 11–16

Chhetri, S. P. Samanta, N. C. Murmu, S. K. Srivastava, and T. Kuila, (2017) Electromagnetic interference shielding and thermal properties of noncovalently functionalized reduced graphene oxide/epoxy composites, *AIMS Mater Sci*, 4(1): 61–74, 2017

Das,T. R. S. Patra, R. Madhuri, and P. K. Sharma, (2018) Bismuth oxide decorated graphene oxide nanocomposites synthesized via sonochemical assisted hydrothermal method for adsorption of cationic organic dyes, *J Colloid Interface Sci*, 509: 82–93

Deshmukh *K.* (2016) Influence of K2CrO4 Doping on the Structural, Optical and Dielectric Properties of Polyvinyl Alcohol/K2CrO4 Composite Films," *Polymer - Plastics Technology and Engineering*, vol. 55 (3): 231–241

Ghosh,A. C. Kulsi, D. Banerjee, and A. Mondal (2016) Galvanic synthesis of Cu 2-X Se thin films and their photocatalytic and thermoelectric properties, *Appl Surf Sci*, 369: 525–534

Garba I. (2020) Results in Physics In fl uence of tartaric acid concentration on structural and optical properties of CuSe nanoparticles synthesized via microwave assisted method, 17: 1–12,

Gautam A. and S. Ram, (2009) Preparation and thermomechanical properties of Ag-PVA nanocomposite films, *Mater Chem Phys,* 119 (1–2): 266–271

Giribabu, K. R. Suresh, R. Manigandan, E. Thirumal, A. Stephen, and V. Narayanan, (2013) Aqueous based synthesis of Cu5Se4 nanosheets and characterization, *Journal of Materials Science: Materials in Electronics*, 24: 1888–1894

Gurusiddesh, M. B. J. Madhu, and G. J. Shankaramurthy, (2018) Structural, dielectric, magnetic and electromagnetic interference shielding investigations of polyaniline decorated Co0.5Ni0.5Fe2O4 nanoferrites," *Journal of Materials Science: Materials in Electronics*, vol. 29(4): 3502–3509

Han, X. F. Liao, Y. Zhang, Z. Yuan, H. Chen, and C. Xu, (2018) CTAB-assisted hydrothermal synthesis of Cu2Se films composed of nanowire networks," *Mater Lett*, 210: 62–65

Hou X. (2018) The study of morphology-controlled synthesis and the optical properties of CuSe nanoplates based on the hydrothermal method *Mater Sci Semicond Process*, 79:92–98

Ichi Fujisawa J., T. Eda, and M. Hanaya, (2017) Comparative study of conduction-band and valence-band edges of TiO2, SrTiO3, and BaTiO3 by ionization potential measurements," *Chem Phys Lett*, 685: 23–26

Jeevanandam, J. A. Barhoum, Y. S. Chan, A. Dufresne, and M. K. Danquah, (2018) Review on nanoparticles and nanostructured materials: History, sources, toxicity and regulations, *Beilstein Journal of Nanotechnology*, 9 (1): 1050–1074

Joseph J. (2018) Dielectric and electromagnetic interference shielding properties of germanium dioxide nanoparticle reinforced poly(vinyl chloride) and poly(methylmethacrylate) blend nanocomposites," *Journal of Materials Science: Materials in Electronics*, 29 (23): 20172–20188

Karteri, I M. Altun, and M. Gunes, (2017) Electromagnetic interference shielding performance and electromagnetic properties of wood-plastic nanocomposite with graphene nanoplatelets, *Journal of Materials Science: Materials in Electronics*, 28(9): 6704–6711

Kombaiah K., J. J. Vijaya, L. J. Kennedy, and M. Bououdina, (2017) Optical, magnetic and structural properties of ZnFe2O4 nanoparticles synthesized by conventional and microwave assisted combustion method: A comparative investigation, *Optik (Stuttg)*, 129: 57–68.

Lala, S. T. N. Maity, M. Singha, K. Biswas, and S. K. Pradhan, (2017) Effect of doping (Mg,Mn,Zn) on the microstructure and mechanical properties of spark plasma sintered hydroxyapatites synthesized by mechanical alloying, *Ceram Int*, 43(2): 389–2397

Lee, P. Y. S. C. Shei, and S. J. Chang, (2013) Evolution pathways for the formation of Nano-Cu2ZnSnSe 4 absorber materials via elemental sources and isophorondiamine chelation," *J Alloys Compd*, vol. 574: 27–32,

Lin W. Yao, G. Xiong, Y. Yang, H. qing Huang, and Y. fen Zhou, (2017) Effect of silica fume and colloidal graphite additions on the EMI shielding effectiveness of nickel fiber cement based composites, *Constr Build Mater*, 150: 825–832

Liu, C. X. Wang, X. Huang, X. Liao, and B. Shi (2018). Absorption and Reflection Contributions to the High Performance of Electromagnetic Waves Shielding Materials Fabricated by Compositing Leather Matrix with Metal Nanoparticles, *ACS Appl Mater Interfaces*, 10 (16): 14036–14044.

Ma Y. (2017) Hexagonal plate-shaped CuSe nanocrystals by polylol solution chemical synthesis," *Integrated Ferroelectrics*, 181 (1): 102–112,

Mohanapriya M. K. (2020) Dynamic mechanical analysis and broadband electromagnetic interference shielding characteristics of poly (vinyl alcohol)-poly (4-styrenesulfonic acid)-titanium dioxide nanoparticles based tertiary nanocomposites, *Polymer-Plastics Technology and Materials* 59 (8): 847–863

Mondal S. (2016) A strategy to achieve enhanced electromagnetic interference shielding at low concentration with a new generation of conductive carbon black in a chlorinated polyethylene elastomeric matrix," *Physical Chemistry Chemical Physics*, 18 (35): 24591–24599

Mondal S. (2016) A strategy to achieve enhanced electromagnetic interference shielding at low concentration with a new generation of conductive carbon black in a chlorinated polyethylene elastomeric matrix," *Physical Chemistry Chemical Physics*, 18 (35): 24591–24599

Shahzad F. (2020) Electromagnetic interference shielding with 2D transition metal carbides (MXenes).” [Online]. Available: http://science.sciencemag.org/

Rajesh B. Kumar and B. Hymavathi, (2017) X-ray peak profile analysis of solid-state sintered alumina doped zinc oxide ceramics by Williamson–Hall and size-strain plot methods,” *Journal of Asian Ceramic Societies*, 5 (2): 94–103

Maharaz, M. K. Halimah, S. Paiman, N. M. Saiden, and I. M. Alibe, (2018) Influence of solvents and irradiation time on structural and optical properties of cubic PbS nanoparticles, *Int J Electrochem Sci*, 13(10): 9317–9332

Muthu S. and M. Babu Sridharan, (2018) Synthesis and Characterization of Two Dimensional Copper Selenide (CuSe) Nanosheets,” *Mater Today Proc*, 5 (11): 23161–23168

Singh S. C. (2018) Structural and compositional control in copper selenide nanocrystals for light-induced self-repairable electrodes, *Nano Energy*, 51: 774–785

Shinde S. K. (2017) Electrochemical synthesis: Monoclinic Cu2Se nano-dendrites with high performance for supercapacitors, *J Taiwan Inst Chem Eng*, 75: 271–279

Wu, Y. I. Korolkov, X. Qiao, X. Zhang, J. Wan, and X. Fan, (2013) Facile synthesis of CuSe nanoparticles and high-quality single-crystal two-dimensional hexagonal nanoplatelets with tunable near-infrared optical absorption,*J Solid State Chem*. 238: 279–283

Singh, V. Murugadoss, S. Nemala, S. Mallick, and S. Angaiah, (2018) Cu2ZnSnSe4 QDs sensitized electrospun porous TiO2 nanofibers as photoanode for high performance QDSC, *Solar Energy*, 171: 571–579.

Saini,M. S. K. Singh, R. Shukla, and A. Kumar, (2018) Mg Doped Copper Ferrite with Polyaniline Matrix Core–Shell Ternary Nanocomposite for Electromagnetic Interference Shielding, *J Inorg Organomet Polym Mater*, 28 (6):2306–2315

Pasha, S. K. K. Deshmukh, M. B. Ahamed, K. Chidambaram, M. K. Mohanapriya, and N. A. N. Raj (2017) Investigation of Microstructure, Morphology, Mechanical, and Dielectric Properties of PVA/PbO Nanocomposites, *Advances in Polymer Technology*, 36 (3): 352–361

Song W. L. (2014) lexible graphene/polymer composite films in sandwich structures for effective electromagnetic interference shielding, *Carbon N Y*, 66: 67–76

Mechanical Performance of Segregated Carbon Nanotube/Poly(lactic acid) Composite for Efficient Electromagnetic Interference Shielding,” *Ind Eng Chem Res*, 58(11): 4454–4461

Muzaffar, A. M. B. Ahamed, K. Deshmukh, and M. Faisal, (2019) Electromagnetic interference shielding properties of polyvinylchloride (PVC), barium titanate (BaTiO3) and nickel oxide (NiO) based nanocomposites, *Polym Test*. 77: 1-12

Tchouank T. Tekou Carol (2020) X-band shielding of electromagnetic interference (EMI) by Co2Y barium hexaferrite, bismuth copper titanate (BCTO), and polyaniline (PANI) composite, *J Magn Magn Mater*, 501: 1-13

Vallés C. (2019) Graphene/Polyelectrolyte Layer-by-Layer Coatings for Electromagnetic Interference Shielding, *ACS Appl Nano Mater* 2 (8); 5272–5281

Wu H. Y. (2018) Simultaneously improved electromagnetic interference shielding and mechanical performance of segregated carbon nanotube/polypropylene composite via solid phase molding, *Compos Sci Technol*, 156 : 87–94

Xing. D. L. Lu, Y. Xie, Y. Tang, and K. S. Teh, (2020) Highly flexible and ultra-thin carbon-fabric/Ag/waterborne polyurethane film for ultra-efficient EMI shielding, *Mater Des*, vol. 185

Yu H. (2012) Graphene/polyaniline nanorod arrays: Synthesis and excellent electromagnetic absorption properties, *J Mater Chem*, vol. 22(40): 21679–21685

Zhang X. (2016) Ordered multilayer film of (graphene oxide/polymer and boron nitride/polymer) nanocomposites: An ideal EMI shielding material with excellent electrical insulation and high thermal conductivity, *Compos Sci Technol*, 136: 104–110

Zhang X. J. (2014) Enhanced microwave absorption property of reduced graphene oxide (RGO)-MnFe2O4 nanocomposites and polyvinylidene fluoride, *ACS Appl Mater Interfaces*, 6 (10):7471–7478

Zhang Q. , H. Li, Y. Ma, and T. Zhai, (2016) ZnSe nanostructures: Synthesis, properties and applications,” *Prog Mater Sci*, 83: 472–535

Zeng Z. (2017) Ultralight and Flexible Polyurethane/Silver Nanowire Nanocomposites with Unidirectional Pores for Highly Effective Electromagnetic Shielding,” *ACS Appl Mater Interfaces*, 9 (37): 32211–32219